Central European Journal of Energetic Materials
ISSN 1733-7178; e-ISSN 2353-1843

Cent. Eur. J. Energ. Mater. 2021, *18*(2): 199-222; DOI 10.22211/cejem/139155
Article is available in PDF-format, in colour, at:
https://ipo.lukasiewicz.gov.pl/wydawnictwa/cejem-woluminy/vol-18-nr-2/

Research paper

Comparative Study of the Penetration Characteristics of Ni-Al and Pure Cu Shaped Charge Liners

Yingbin Liu[1,*], Chaoxia Zhang[1], Xiaoyan Hu[1], Li Yang[2], Miao Sun[3], Zeng Zhang[1], Lei Yuan[4]

[1] *School of Environment and Safety Engineering, North University of China, Taiyuan 030051, China*
[2] *Military Products Research Institute, Shanxi Jiangyang Chemical Co. Ltd., Taiyuan 030051, China*
[3] *Hypervelocity Impact Research Center, Harbin Institute of Technology, Harbin 150080, China*
[4] *Beijing Special Vehicle Research Institute, Beijing 100072, China*
* *E-mail:* ybliu@nuc.edu.cn

Abstract: In order to investigate the correlation between the reactivity of Ni-Al and micro-structural differences in the crater walls, penetration experiments were performed with Ni-Al and pure Cu shaped charge liners (SCLs). The experimental results showed that the average penetration depth of Cu jets is 2.3 times that of Ni-Al jets, but the crater entrance diameter of Ni-Al jets is larger by 26.6%. The microstructure of the recovered targets was characterized using optical microscopy, scanning electron microscopy, energy dispersive spectroscopy, and a Vickers micro-hardness system. The Ni-Al "white" band was thicker than that of Cu because it releases a lot of heat. The micro-hardness test showed that the "white" band had a relatively high hardness, and the "white" band hardness in the tail was more significant than that in the head. However, the micro-structural evolution of the crater walls is related to the reactivity of Ni-Al, but is also related to other factors. Combined with the macro penetration results and the evolution of the micro-structure of the crater walls, the "white" band can absorb impact energy more strongly and weaken the jet breaking ability or armour protection ability.

These results can provide more valuable reference for designing shaped charge warheads and protection structures.

Keywords: shaped charge liner, Ni-Al, penetration experiments, "white" band, micro-structure analysis

1 Introduction

Energetic structural materials (ESMs) are a new kind of multifunctional composite material with the dual functions of structural strength and energy release characteristics. Therefore, ESMs have comprehensive application prospects in military fields, such as reactive fragments [1-3], reactive shaped charge liners [4-6], and reactive armour [7, 8]. Shaped charge liners made of reactive materials can achieve improved damage effects by incorporating kinetic energy and chemical energy.

Nickel-aluminum (Ni-Al) composites belong to typical energetic structural materials. They have mechanical properties equivalent to ordinary metallic materials and can cause chemical reactions to release a large amount of heat. Over the past two decades, extensive research work has been performed on Ni-Al reactive metal composites. Smith *et al.* [9] discussed the effects of voids and particle friction on the mechanical properties and thermal response of Al/Ni composites under shock and compressive loading through mesoscale simulations. Bacciochini *et al.* [10] improved the reactivity of Ni-Al energetic materials through ball-milling technology, and retained the high reactivity features of Ni-Al powder on the substrate through cold spray technology. Zhou *et al.* [11] studied the quasi-static and dynamic compressive behaviour and energetic characteristics of the fully dense Ni-Al ESM prepared by explosive consolidation. The results showed that the Ni-Al ESM has a high compressive strength of 300 MPa and a ductility of 14.5%. In addition, at an impact velocity above 671 m/s, the Ni-Al ESM was initiated and released increased impact temperature or energy. Zhang *et al.* [12] investigated the energy release characteristics and mechanical properties of bulk Ni-Al (molar ratio of 1:1) ESM fabricated by cold-pressing and sintering with nickel and aluminum powders. The results demonstrated that Ni-Al ESMs with excellent strength and energy density could be obtained when the sintering temperature was 550 ºC. Xiong *et al.* [13] carried out impact initiation experiments on Al/Ni composites. They also investigated the influence of cold-rolling and powder compaction on the shock-induced chemical reaction (SICR) behaviour of Al/Ni composites. The results revealed that Al/Ni powder composites have the highest energy release capability.

The interactions in the Ni-Al system was also intensely studied by many researchers, and data on the phase diagram of this system were analyzed in considerable detail [14-16]. Ni-Al reactive materials will form five intermetallic compounds at different temperatures or different shock loads: NiAl, $NiAl_3$, Ni_3Al, Ni_2Al_3, and Ni_3Al_2. The NiAl intermetallic compound has a cubic crystal structure (CsCl structure type) with a space group Pmm. The NiAl homogeneity range extends from 42.5 to 69.6 wt.% of Ni at high-temperatures. NiAl with a sufficiently wide homogeneity range is the only congruently melting compound, and the main product under high impact conditions. The heat of reaction of Ni-Al reactive materials (the heat of reaction per unit mass/volume is 1381 J/g and 7158 J/cm^3) is equivalent to TNT, and the adiabatic reaction temperature is 1910 K [17]. Turrillas *et al.* [18] monitored the synthesis of NiAl from thermally activated equimolar powder mixtures of Ni and Al; the reaction was found to occur through melting of Al and the subsequent dissolution of Ni to form the NiAl. The results showed that the greatest thermal effect and the highest temperature are reached in equi-atomic compositions. If there is an excess of Ni, a substitutional solid solution is formed, and Al atoms are statistically substituted by Ni atoms. If there is an excess of Al, an omission solution is formed, and defects are formed in the structure. Additionally, initiation of such reactions by a shock wave may enhance the reaction rate by many orders of magnitude, up to the so-called solid-phase detonation [19, 20].

The penetration of a reactive liner shaped charge jet (RLSCJ) has significant research value because it involves dynamic super-plastic deformation and energetic characteristics. Studies indicate that in the penetration of a RLSCJ, there are coupled factors such as impact compression characteristics, impact temperature-rise, SICR, energy release characteristics, and the interaction between the shaped charge jet and the target, so this process is very complicated. The penetration performance of shaped charge jets mainly includes the macroscopic penetration effect (penetration depth and hole diameter) and microstructure characteristics. Wang Haifu's research group [6, 21, 22] fabricated PTFE/Al reactive liners, double-layered liners (inner copper liner and outer PTFE/Al reactive material liner), and PTFE/W/Cu/Pb high-density reactive liners *via* a cold-pressing/sintering process, and studied the penetration performance of RLSCJs impacting thick steel targets. The experimental results demonstrated that the PTFE/Al reactive jet exhibits a relatively larger hole diameter and lower penetration depth than the traditional copper jet. Compared with the PTFE/Al reactive jet, the reactive material-copper jet has a deeper penetration depth and a larger hole diameter. The penetration depth of PTFE/W/Cu/Pb reactive jets initially increased and then decreased

on increasing the standoff. When the standoff was 1.5 CD (charge diameter), the penetration depth of this high-density reactive jet was significantly higher than that of the PTFE/Al reactive jet. Compared with a copper jet, the entrance hole diameter caused by this high-density reactive jet was increased by 29.2% at the same standoff. Despite their high energy density, the low density, low sound velocity, and low strength of PTFE-based reactive materials, their applications are limited. Therefore, the Ni-Al reactive metal materials, with good mechanical properties and high energy density, are more suitable for shaped charge liner materials. However, there are few studies on the damage performance of Ni-Al reactive shaped charge liners. Church *et al.* [5] investigated the Ni-Al reactive shaped charge liner. XRD analysis indicated that the Ni-Al shaped charge jet had reacted during the formation process to produce intermetallic compounds. Byun *et al.* [23, 24] sprayed reactive Al-Ni composites on a well-penetrating Cu liner by a kinetic spray process, and enhanced the exothermic reaction of the reactive layer by controlling the structure of the feedstock material to enhance the penetration ability and explosive power of shaped charge liners. Sun *et al.* [25] studied the penetration performance of Ni-Al and Cu-Ni-Al reactive shaped charge liners. The results showed that the penetration depth of the Cu-Ni-Al reactive liner was increased by 42% compared to the Ni-Al reactive liner, and the entrance hole diameter had also been improved. A "white" band was found on the crater walls.

Microstructure evolution of metallic materials is a common phenomenon under high strain rates, such as penetration, high-speed impact, and explosion. It is generally believed that there are two mechanisms of evolution for metallic materials during dynamic plastic deformation: hardening (such as strain hardening or strain rate hardening) and softening (such as thermal softening). In the near adiabatic penetration process, the heat generated by rapid deformation cannot be diffused in time. As the strain localization intensifies, the microstructure of the targets changes. Yin *et al.* [26] analyzed the microstructure characteristics of crater walls penetrated by shaped charge jets. The results demonstrated that phase transformation took place in the "white" etching layer due to the extremely high temperature on the crater walls. The microstructure of the "white" etching layer is a mixture of martensite and austenite. The values of micro-hardness of the "white" etching layer is lower than those of untempered martensite steel due to the cooling rate being very high. In earlier research, the "white" band on the crater walls of a steel target penetrated by Ni-Al and Cu-Ni-Al shaped charge jets was investigated [25]. The "white" zones in the tail were thicker than those in the head. The micro-hardness values in the head were higher than those in the tail. They attributed this phenomenon to the exothermic reaction of Ni-Al.

However, whether this phenomenon is related to the exothermic behaviour of the reactive material remains to be verified.

In the present research, the macroscopic penetration characteristics and microstructural characteristics of steel targets penetrated by pure Cu jets and Ni-Al (66:34, wt.%) reactive jets were compared and analyzed. Subsequently, the relationship between the reactivity of the Ni-Al ESM and the microstructural differences between the head and the tail of the crater walls was explored. This further revealed the key factors that lead to microstructure evolution. The influence of microstructure evolution on a semi-infinite steel target is discussed.

2 Materials and Methods

Ni, Al, and Cu powders, as the raw materials, were used to prepare the Ni-Al reactive shaped charge liners (RSCL) and traditional Cu shaped charge liners (TSCL) of the same size. Figure 1 shows the distinct particle morphology and size of the three powders. The physical properties of the powders are listed in Table 1.

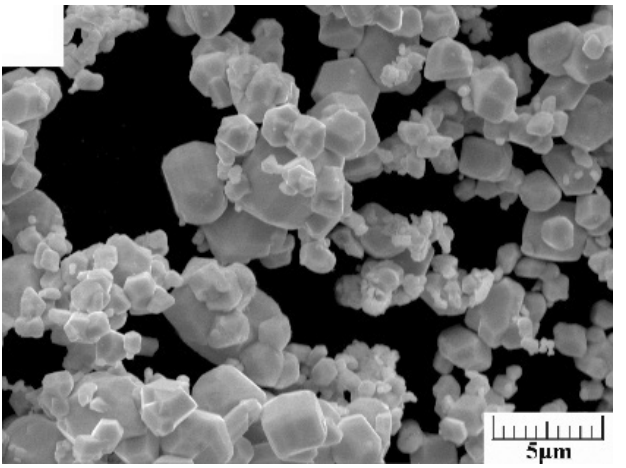

(a)

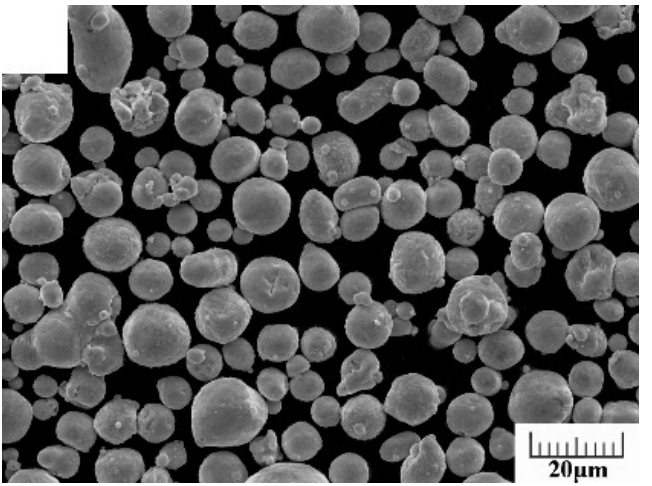

(b)

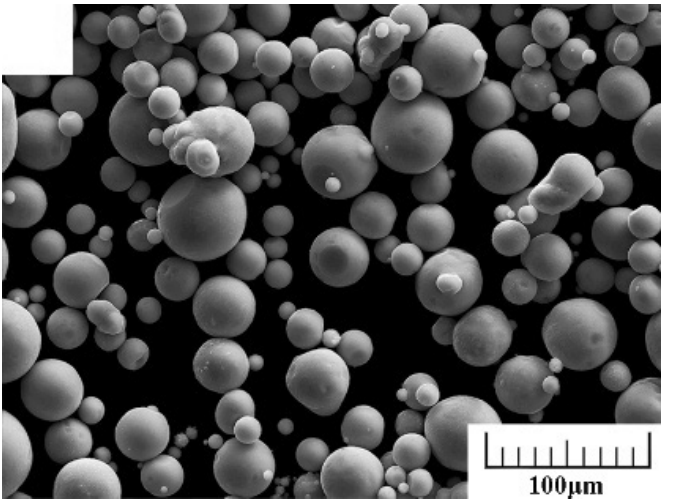

(c)

Figure 1. SEM images of the raw materials for the SCLs: (a) Ni, (b) Al, (c) Cu

Table 1. The properties of the powders

Powder material	Shape	Size [μm]	Purity [pct]
Ni	angular rounded	2-6	99.9
Al	rounded	6-15	99.9
Cu		20-50	99.9

The RSCLs, with a Ni:Al mass ratio of 66:34, were fabricated by the powder compact method, see Figure 2(a). The TSCLs, composed of pure Cu powder, were also prepared by the same process, as shown in Figure 2(b). The tailored conical SCLs were theoretically 47 mm in height and 1.8 mm in thickness, with a cone angle of 47°. The dimensions and other physical properties are listed in Table 2. AMD refers to the actual material density of the SCLs, and was measured by the Archimedes method. The theoretical maximum density (TMD) was calculated for the RSCLs according to the mass fractions of the material components. By comparing the theoretical and the measured densities, the porosity of the two groups of SCLs could be calculated through the relation (Equation 1), and are listed in Table 2.

$$P = 1 - \frac{AMD}{TMD} \tag{1}$$

As seen, the RSCLs and the TSCLs have almost the same dimensions and porosity, but the RSCLs were about 44.5% lighter than the TSCLs.

(a)

(b)

Figure 2. The pressed liners of (a) Ni-Al RSCLs, (b) Cu TSCLs

Table 2. The relevant parameters of the SCLs

SCL	Number	[wt.%]	Mass [g]	TMD [g/cm^3]	AMD [g/cm^3]	Height [mm]	Thickness [mm]	Porosity [%]
Ni-Al	RSCL-1	66:34	27.54	5.00	4.73	47.01	1.72	5.4
	RSCL-2		27.91	5.00	4.76	46.39	1.78	4.8
	RSCL-3		27.43	5.00	4.75	46.87	1.70	5.0
Cu	TSCL-1	1	49.85	8.90	8.35	46.93	1.72	6.2
	TSCL-2		49.37	8.90	8.30	46.58	1.69	6.8
	TSCL-3		50.01	8.90	8.28	47.10	1.75	7.0

The physical picture of the shaped charge device is shown in Figure 3. Figure 4 shows the assembly drawing of the cross-sectional view of the shaped charge device. The metal casing was made of 45# steel. The charge diameter (CD) and the liner diameter (LD) were both 44 mm. All of the SCLs were tested under the same conditions, including the standoff and the composition of the explosive. For 8# electric detonator initiated shaped charge devices, the standoff was 60 mm. The target in the penetration experiments was 45# steel. A schematic illustration of the penetration experiment is shown in Figure 5.

Figure 3. The physical picture of the shaped charge device

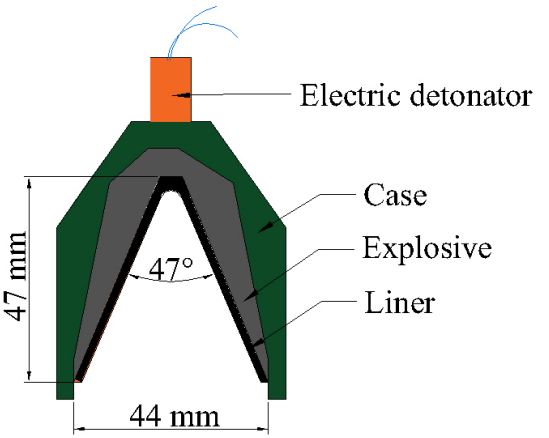

Figure 4. Schematic illustration of the shaped charge device with the SCL

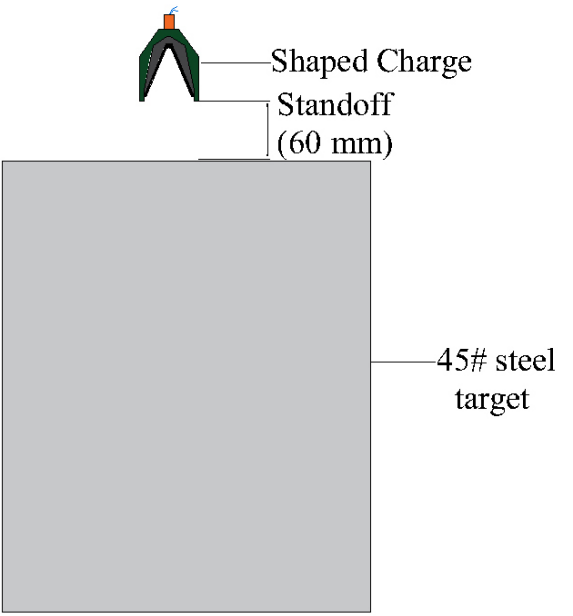

Figure 5. Schematic illustration of the penetration experiment for SCLs

The targets were recovered and cleaned after the penetration tests in order to analyze the penetration characteristics of the SCLs. The recovered targets were longitudinally cut along the centerline of the ballistic perforations by electrical discharge machining. Samples of the cross-section were then cut from

the head and tail sections of the crater walls. The red squares in Figure 6 marks the sampling points. The samples were well polished and etched with a solution composed of water (100 mL) and nitric acid (4 mL) for microanalysis. In order to examine the relationship between the testing observations and the experimental data, the microstructure investigations of these samples were performed using an Axio Lab A1 optical microscope (CarlZeiss, Jena, Germany) and scanning electron microscope (SEM). To investigate the microstructural characteristics of the materials distributed in the different zones, the hardness of the samples was examined using a Vickers micro-hardness system (JMHVS-1000AT) at a load of 0.98 N (100 gf) for 15 s.

3 Results

Figure 6 displays a typical sectional view of the targets penetrated by a Ni-Al RSCL and a traditional Cu SCL. As seen, the sectional shape of the penetration hole is close to a trumpet shape. It was found that the average crater entrance diameter of TSCLs was about 15.2 mm, and the crater walls were very smooth, as compared to that of the RSCLs. For the penetration hole of the RSCLs, the average crater entrance diameter was about 20.7 mm, which is 26.6% larger than that of the TSCLs. In addition, it was observed that the crater walls penetrated by the RSCLs were very rough, which should be attributed to the exothermic reaction between the Ni and Al powders occurring during the penetration process. However, the average penetration depth of RSCLs was about 76 mm, while for the TSCLs it was about 175 mm. The smaller density and the reaction of the materials during the penetration process should reduce the penetration depth. The experimental data are listed in Table 3.

Table 3. Penetration parameters of the targets penetrated by the different SCLs

SCL	Number	Penetration depth [mm]	Average penetration depth [mm]	Crater entrance diameter [mm]	Average crater entrance diameter [mm]
Ni-Al	RSCL-1	71	76	21.0	20.7
	RSCL-2	81			
	RSCL-3	77		20.0	
Cu	TSCL-1	182	175	16.0	15.2
	TSCL-2	175		14.5	
	TSCL-3	169		15.0	

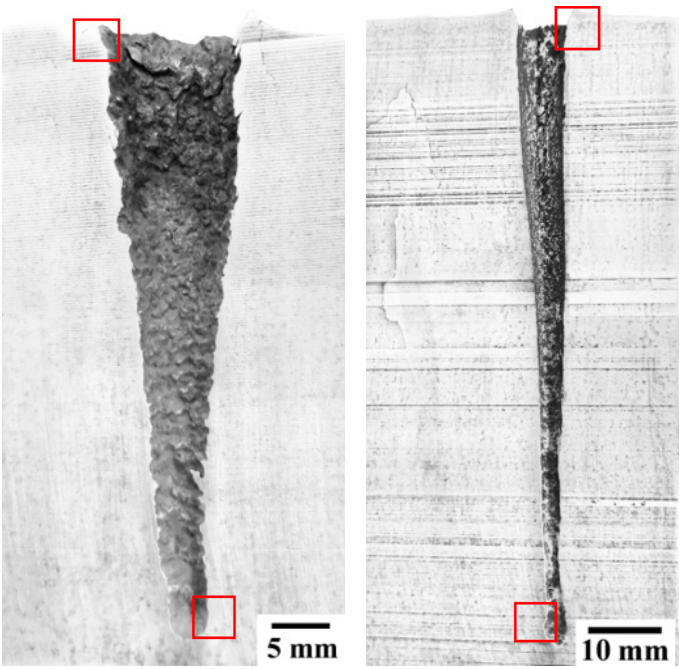

Figure 6. Macroscopic features of the targets penetrated by (a) Ni-Al, and (b) Cu jet

Figure 7 is a schematic of the regions where the hardness and microanalysis were carried out. The residual jet was attached to the crater walls. The influence of the shaped charge jet on the steel target was mainly the crater walls and the 0-2 mm regions around the crater. Therefore, different influence zones after the penetration have been investigated.

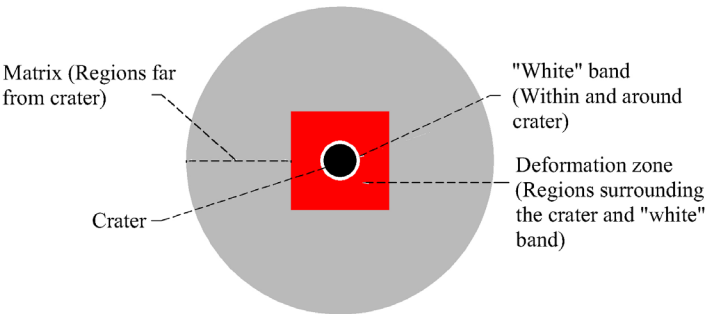

Figure 7. Schematic of the regions on the targets for hardness and microanalysis

Figure 8 displays optical micrographs of the specimens extracted from the head (Figures 8(a) and 8(b) and the tail (Figures 8(c) and 8(d)) of the crater walls generated by the Ni-Al jet. The colour bars of the images mark the distribution regions of the residual jet (red), "white" band (yellow), deformation zone (blue), and the matrix (green). The "white" band in the head of the crater walls was about 30-80 μm, while the "white" band in the tail increased to about 210-340 μm. Figure 9 illustrates the optical micrographs of the specimens extracted from the head (Figures 9(a) and 9(b)) and the tail (Figures 9(c) and 9(d)) of the crater walls generated by the Cu jet. The colour bars of the images mark the distribution regions of the residual jet (red), "white" band (yellow), deformation zone (blue), micro-cracks (orange), and the matrix (green). For the Cu jets, the "white" band was not evident in the head of the crater walls. However, there are many micro-cracks, about 1.5-2.0 mm, around the crater wall. The orientation of the cracks was mainly parallel to the penetration direction. In the tail of the crater walls, an obvious "white" band can be observed, and the thickness of the "white" band was about 120-180 μm. Table 4 summarizes the thickness parameters of the affected zones in the targets penetrated by the different SCLs. Figure 10 shows the SEM/EDS line analysis results of the Ni-Al and Cu residual zones and the "white" zones, and Figure 11 shows the SEM/EDS area analysis results of the Ni-Al and Cu residual zones and "white" zones. It can be seen that there is almost no Fe element in the Cu residual jet, while the percentage of Fe in the Ni-Al residual jet is very high.

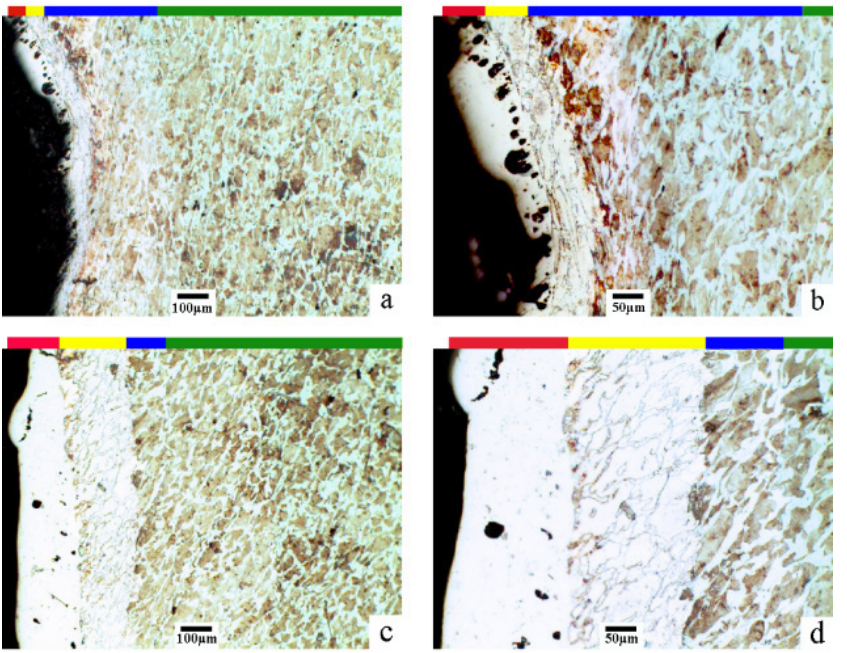

Figure 8. Optical microscope images of the crater walls of the targets penetrated by the Ni-Al jet: (a) the head of the crater walls (100×), (b) the head of the crater walls (200×), (c) the tail of the crater walls (100×), and (d) the tail of the crater walls (200×)

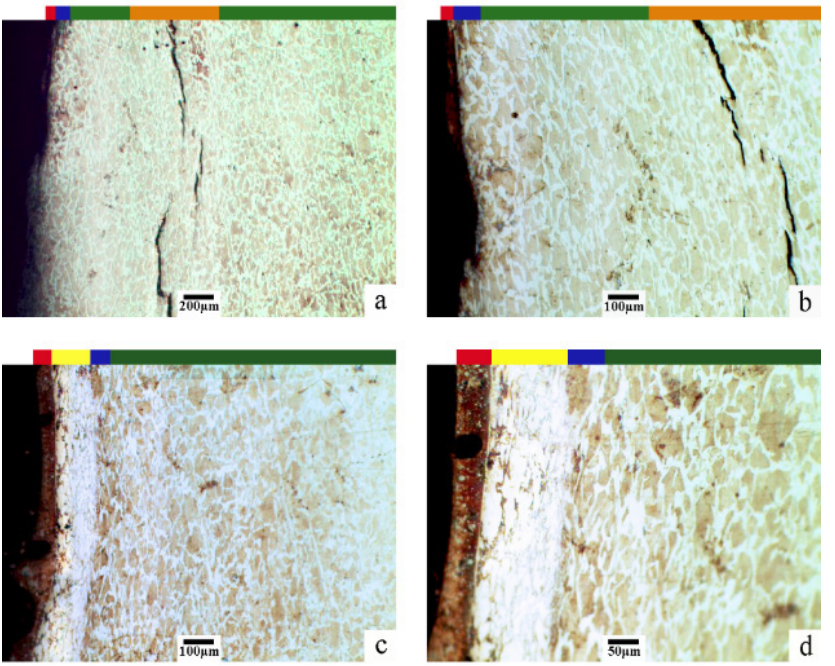

Figure 9. Optical microscope images of the crater walls of the targets penetrated by the Cu jet: (a) the head of the crater walls (50×), (b) the head of the crater walls (100×), (c) the tail of the crater walls (100×), and (d) the tail of the crater walls (200×)

Table 4. Thickness parameters of the affected zones in the targets penetrated by different SCLs

SCL	Part of target	Residual jet zone [μm]	"White" band [μm]	Deformation zone [μm]	Micro-crack zone [μm]	Total affected zone [μm]
Ni-Al	Head	10-110	30-80	110-160	–	150-350
	Tail	40-170	210-340	50-90	–	300-600
Cu	Head	10-30	0	50-80	350-400	410-530
	Tail	40-70	120-180	50-110	–	210-360

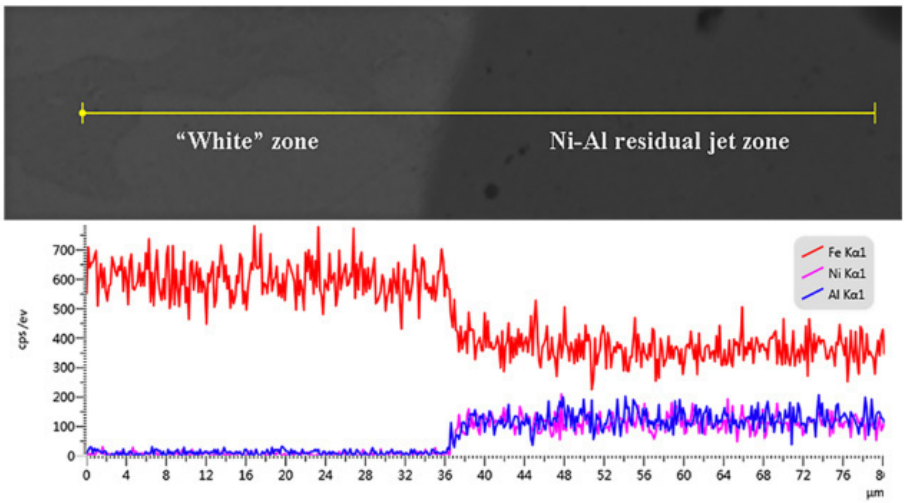

(a)

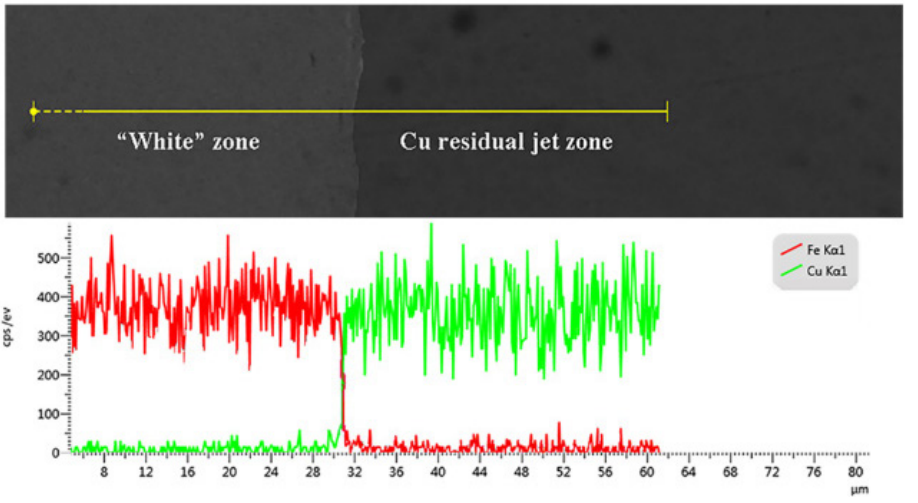

(b)

Figure 10. The SEM/EDS line analysis of (a) Ni-Al residual zone and "white" zone, and (b) Cu residual zone and "white" zone

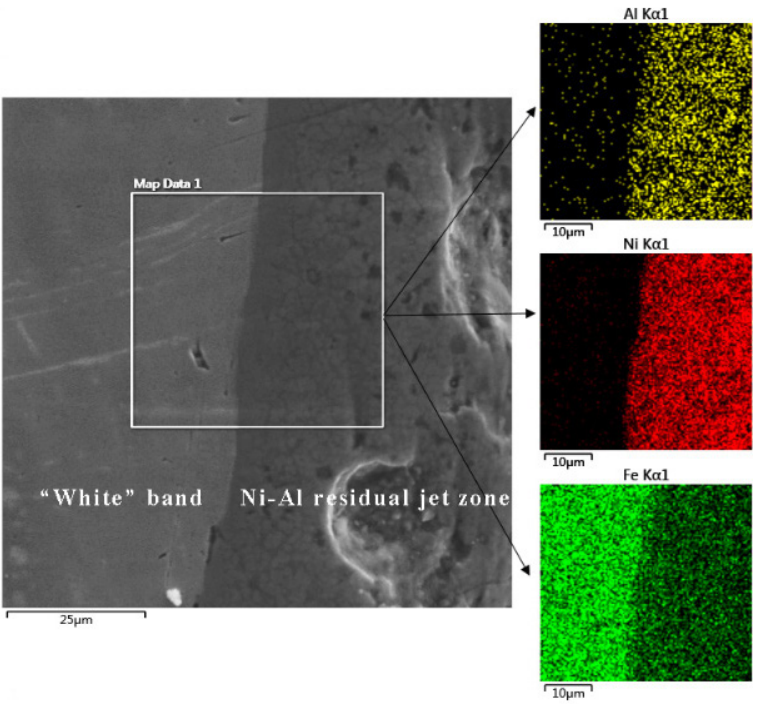

(a)

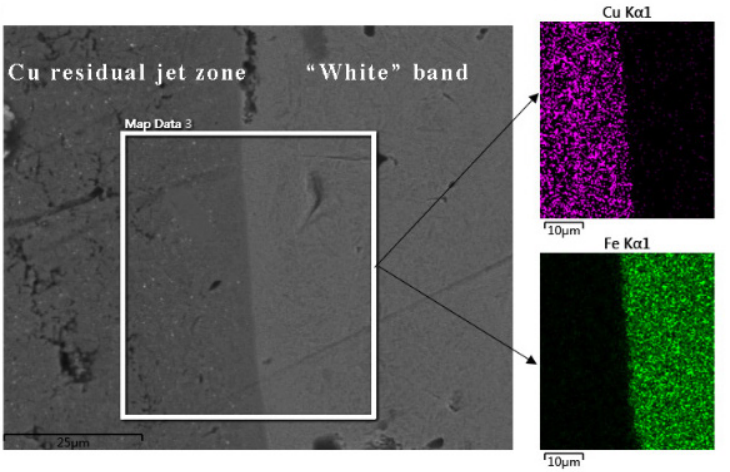

(b)

Figure 11. The SEM/EDS area analysis of (a) Ni-Al residual zone and "white" zone, and (b) Cu residual zone and "white" zone

Figure 12 illustrates the Vickers micro-hardness values in the head and tail of the crater walls generated by the two different SCLs. The micro-hardness change trends in the head and tail of the crater walls penetrated by the two different SCLs were the same. Compared with other zones, the "white" zone has a higher hardness. The micro-hardness values of the "white" band in the tail were higher than those in the head. The difference between the hardness values of the Ni-Al "white" zone in the head and tail was massive, while the hardness values of the "white" zone in the tail was twice those in the head. The micro-hardness values of the Cu "white" band in the tail were increased by 20% compared to those in the head. The micro-hardness values of the Ni-Al "white" band in the tail were increased by 260 HV compared to those of Cu, and the hardness values of the Ni-Al "white" band in the head were decreased by 80 HV compared to those of Cu. The micro-hardness values of the Ni-Al residual jet zone were higher than those of Cu. The hardness values of the Ni-Al plastic deformation zone in the tail were higher than those in the head, while the Cu values were the reverse.

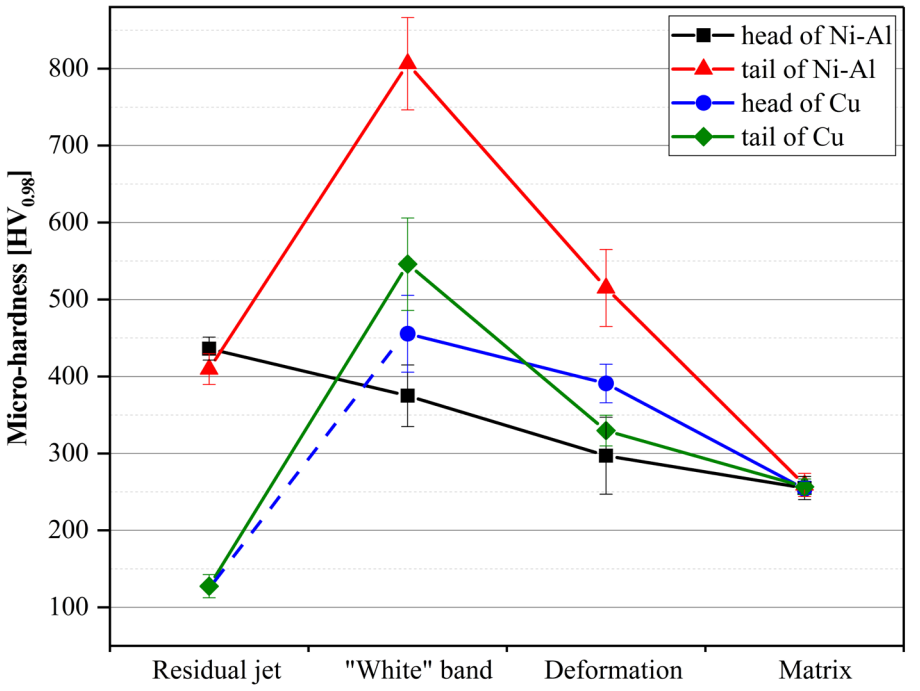

Figure 12. The Vickers micro-hardness values of the crater walls penetrated by the two SCLs

4 Discussion

Powders with different particle sizes used to prepare the Ni-Al RSCLs can effectively reduce the porosity and avoid excessive advance reaction due to the collapse of the reactive liners, which dramatically affects the penetration depth. In the penetration process, the interaction between the jet and the target is an essential factor affecting its penetration performance [27, 28]. Combining the smoothness of the crater wall and the SEM/EDS analysis results, the Fe content in the residual jet can indicate the strength of the interaction between the jet and the crater wall. Therefore, Cu plays a lubricating effect between the jet and the crater walls, and the interaction between the jet and the crater walls is limited. Compared with the Cu jet, the interaction between the Ni-Al reactive jet and the crater walls was violent, resulting in lateral energy dissipation of the Ni-Al jet. Consequently, the average penetration depth of the Cu jets was 2.3 times that of the Ni-Al jets. However, the crater entrance diameter of the Ni-Al jets was larger by 26.6%.

4.1 Analysis of the "white" band

Since the powder liners are not prone to slugs, this avoids the influence of additional heat on the crater wall. It has been beneficial to analyze the "white" band on the entire crater wall. When the shaped charge jet impacts the target, the shock wave causes a significant change in the crater walls [29]. The shaped charge jet transfers energy and pressure to the target through the coupling. Under the combined action of shear and lateral compression, it is easier for 45# steel to produce "white" bands. Although the reasons for the formation of the "white" band have not been established, this requires a certain amount of energy. At a small standoff, we assume that the spatial distribution of the jet velocity is linear, and the virtual origin theory can accurately predict the penetration. In the linear velocity rod penetration model, Lambert [30] calculated the energy deposited in the unit penetration depth of the jet with a velocity gradient, the relationship being as follows:

$$\frac{dE}{dP} = \frac{\gamma m_0 {V_{j0}}^3}{2(V_{j0} - V_r)z_0}\left(\frac{P}{z_0}\right)^{-(1+3\gamma)}$$
$$\gamma = \sqrt{\frac{\rho_t}{\rho_j}} \quad (2)$$

where m_0 is the initial mass of the jet, ρ_j and ρ_t are the densities of the jet and target respectively, P is the penetration depth, V_{j0} and V_r are the tip and tail velocities of the jet, and z_0 is the distance from the virtual origin to the target.

According to the above formula, density is a critical factor. In the initial penetration stage, low-density material deposits more energy, the penetration depth is lower, and the crater entrance diameter is more extensive. High-density material deposits less energy and can bring more kinetic energy into the target. For steel targets, the energy deposition of the Cu jet was lower, while the Ni-Al jet was higher.

Usually, the velocity of shaped charge jets is very high, and can generate too high a pressure and temperature after hitting the target. The plastic deformation and strain rate of the target tissue around the crater wall is also tremendous. The strain rate is about 10^4-10^6 s^{-1}. There is a region of high temperature, high pressure, and high strain rate around the crater wall, where the "white" band production occurs quickly. In the plastic deformation process, the thickness of the "white" band is related to strain, strain rate, and temperature. When the strain rate is higher, the stress will increase as the strain rate increases. For the same target, the thickness of the "white" band under a higher strain rate and strain will be reduced. Bai *et al.* [31] proposed an approximate formula for calculating the half-width (δ) of the band:

$$\delta \sim \sqrt{\lambda T/\tau\dot{\gamma}} \quad (3)$$

where λ is thermal conductivity, T is temperature, τ is strain and $\dot{\gamma}$ is strain rate.

In the initial stage of jet penetration, the effects of strain and strain rate are more potent than that of the tail. But at the same small standoff, the velocity of the two jets exhibited no difference when impacting the target. Therefore, the thickness of the "white" band in the head of the crater walls was mainly affected by the temperature. Due to the Ni-Al ESM releasing a large amount of heat, the temperature exhibited a more considerable influence on the target tissue around the crater walls penetrated by the Ni-Al

reactive jet. Therefore, the "white" band in the head of the walls was thicker than with the Cu jet. The crater walls in the head of the Cu jet showed no trace of a "white" band, as indicated in Figure 9. This indicates that there is a threshold for the formation of a "white" band. Although there is enough deposition energy, and the strain and strain rate are large enough, the temperature is relatively low, and the "white" band cannot form.

During penetration, the energy and velocity of the jet are gradually attenuated. The effects of the strain and strain rate on the crater walls gradually decreases, creating conditions for the formation of the "white" band. So the "white" band in the tail was thicker than that in the head, as highlighted in Figures 8 and 9. Since the entire penetration process is maintained for only a few microseconds, the temperature change of the Cu jet could be ignored. Due to the exothermicity of the Ni-Al ESM, the Ni-Al "white" band in the tail is thicker than for the TSCLs.

4.2 Micro-hardness analysis

The target has different levels of shock wave response in the direction of jet penetration and lateral compression. In addition, crystal defects, such as dislocations and twins, increase the hardness of materials, similar to explosion hardening. However, the crater walls experience a very high temperature under the combined action of plastic deformation temperature-rise and jet temperature. Thermal softening will gradually become a main advantage. The "white" zone was very narrow compared to the entire target and can be cooled quickly by the surrounding environment, the cooling time being about 1-10 ms, which is similar to a quenching process. So, a martensitic transformation took place. The SEM/EDS analysis results and the hardness measurements also confirmed this view [25]. Therefore, the micro-hardness values of the "white" band were higher than those of the surrounding tissue. Because the cooling rate was too high, austenite cannot convert entirely into martensite. Therefore, the "white" band is austenite and martensite mixtures, and the hardness values were lower than for pure martensite steel [21, 26].

In the initial stage of jet penetration, the "white" band softens due to the target tissues absorbing a lot of energy. Therefore, the micro-hardness values of the "white" band were lower than those in the tail, as shown in Figure 12. Compared to the Cu jet, the Ni-Al reactive jet has a higher temperature and more severe lateral energy dissipation, resulting in a higher thermal degree of softening of the "white" zone, so the micro-hardness values are decreased. In the tail of the crater walls, because the additional heat release of the Ni-Al jet caused more austenite to transform into martensite, the micro-hardness values of the "white" band were higher than those from Cu. The plastic deformation zone

is in the hardening stage. The influence of the strain and strain rate on the crater walls are gradually reduced as the jet penetrates. Therefore, the hardness values of the Cu deformation zone in the tail were lower than those in the head. However, this caused secondary hardening of the deformation zone due to the additional heat release by the Ni-Al jet. So the micro-hardness values of the Ni-Al deformation zone in the tail are increased. The Ni-Al jet has reacted during the formation process to produce intermetallic compounds, so the hardness values of the Ni-Al residual jet zone were higher than those of Cu.

According to the above analysis, the exothermic behaviour of Ni-Al affected the micro features of the "white" band. However, the evolution trend of the microstructures of the inert Cu jets and the Ni-Al reactive jets was the same. Both "narrow-head and wide-tail" and "soft-head and hard-tail" were exhibited. Therefore, the important factor is the localization and size of the strain, and the temperature rise does not seem to be that important.

4.3 The influences of the "white" band on semi-infinite steel targets

For semi-infinite steel targets, the average penetration depth of a Cu jet was higher, as illustrated in Figure 6. However the thickness of the "white" band in the head was only about 0-5 μm, and the strong shearing created many micro-cracks, about 1.5-2 mm, around the crater wall, as shown in Figures 9(a-b). As highlighted in Figures 8 and 9, the Ni-Al "white" band was thicker than that of Cu, but the average penetration depth was lower. This indicates that the "white" band absorbed a lot of energy. In other words, "white" bands are a strong manifestation of the energy released by the targets. Therefore, it is necessary to reconsider the effect of bands on the fracture behaviour of the targets. During the penetration process, the formation of a "white" band can coordinate the deformation of the surrounding regions to prevent the material from prematurely breaking due to instability. Steel materials have a high thermal conductivity. The "white" band formed at a high-temperature, and was then quickly cooled, resulting in high strength of the "white" band so that it can withstand high fracture stress. For semi-infinite steel targets, the "white" band absorbed a large amount of impact energy and impeded jet penetration. Therefore, combined with the macro penetration results and the microstructure evolution of the crater walls, the "white" band can absorb the impact energy more strongly and thus weaken the jet breaking ability or armour protection ability.

5 Conclusions

In our study, the penetration characteristics of Ni-Al and pure Cu shaped charge liners were compared and analyzed. The relationship between the exothermic reaction of Ni-Al ESMs and the microstructure evolution of the crater walls was also investigated. Several conclusions are presented as follows:

- Compared with traditional Cu shaped charge liners, the experiments showed that Ni-Al RSCLs impacting 45# steel targets produced lower penetration depth, but the crater entrance diameter was increased by 26.6%.
- Examination of the microstructure showed that its evolution in the crater walls as generated by inert Cu SCLs and Ni-Al RSCLs was the same. The "white" band from the two kinds of jets showed the phenomena of "narrow-head and wide-tail" and "soft-head and hard-tail". The exothermicity of a Ni-Al ESM can change the thickness and micro-hardness of the "white" band. However, the size and localization of plastic deformation are essential factors in the evolution of the microstructure of the crater walls.
- Combined with the macro penetration characteristics of the two SCLs and the evolution of the microstructure of the crater walls, it can be seen that the "white" band can absorb a lot of the strong-load impact energy and hinder jet penetration.

Acknowledgment

The authors would like to acknowledge the technical support of Professor Tiansheng Liu for technical guidance. The authors would also like to acknowledge financial support from the National Natural Science Foundation for Young Scientists of China (No. 11802274), the National Natural Science Foundation for Young Scientists of China (No. 12002319) and Key Laboratory Open Research Foundation of North University of China (DXMBJJ2018-01).

References

[1] Lee, R.J.; Mock, W.; Carney, J.R.; Holt, W.H.; Pangilinan, G.I.; Gamache, R.M.; Boteler, J.M.; Bohl, D.G.; Drotar, J.; Lawrence, G.W. *Reactive Materials Studies. Shock Compression of Condensed Matter, AIP Conf. Proc*. **2006**, *845*: 169-174.

[2] Chen, J.; Chen, Y.J.; Li, X.; Liang, Z.F.; Zhou, T.; Xiao, C. Metallic Reactive Materials Application in Fragmentation Warhead. *J. Phys.: Conf. Ser*. **2020**, *1507*: 062004.

[3] Wang, S.; Kline, J.; Miles, B.; Hooper, J. Reactive Fragment Materials Made from an Aluminum-Silicon Eutectic Powder. *J. Appl. Phys.* **2020**, *128*(6): 065903.

[4] Bates, L.R.; Bourne, B. *Oil Well Perforators.* Patent US 8220394, **2012**.
[5] Church, P.; Claridge, R.; Ottley, P.; Lewtas, I.; Harrison, N.; Gould, P.; Braithwaite, C.; Williamson, D. Investigation of a Nickel-Aluminum Reactive Shaped Charge Liner. *J. Appl. Mech.-T. Asme*. **2013**, *80*(3): 031701.
[6] Wang, H.; Guo, H.; Geng, B.; Yu, Q.; Zheng, Y. Application of PTFE/Al Reactive Materials for Double-Layered Liner Shaped Charge. *Materials* **2019**, *12*(17), paper 2768: 1-18.
[7] Mayseless, M. Effectiveness of Explosive Reactive Armor. *J. Appl. Mech*. **2011**, *78*(5): 748-760.
[8] Micković, D.; Jaramaz, S.; Elek, P.; Miloradović, N.; Jaramaz, D. A Model for Explosive Reactive Armor Interaction with Shaped Charge Jet. *Propellants Explos., Pyrotech*. **2016**, *41*(1): 53-61.
[9] Smith, G.; Bardenhagen, S.; Nairn, J. Mesoscale Modeling of Al/Ni Composites. *Int. J. Impact Eng*. **2020**, *140*, paper 103537: 1-7.
[10] Bacciochini, A.; Bourdon-Lafleur, S.; Poupart, C.; Radulescu, M.; Jodoin, B. Ni-Al Nanoscale Energetic Materials: Phenomena Involved During the Manufacturing of Bulk Samples by Cold Spray. *J. Therm. Spray Techn.* **2014**, *23*(7): 1142-1148.
[11] Zhou, Q.; Hu, Q.; Wang, B.; Zhou, B.; Chen, P.; Liu, R. Fabrication and Characterization of the Ni-Al Energetic Structural Material with High Energy Density and Mechanical Properties. *J. Alloy Compd*. **2020**, *832*, paper 154894: 1-11.
[12] Zhang, D.; Wang, T.; Yu, Y.; Pan, J.; Wang, W. Preparation and Properties of Ni-Al Energetic Structural Material. *Rare Metal Mat. Eng*. **2017**, *46*(11): 3469-3473.
[13] Xiong, W.; Zhang, X.; Zheng, L.; Bao, K.; Guan, Z. The Shock-Induced Chemical Reaction Behaviour of Al/Ni Composites by Cold Rolling and Powder Compaction. *J. Mater. Sci*. **2019**, *54*(1): 6651-6667.
[14] Zhukov, A.N.; Yakushev, V.A.; Ananev, S.Y.; Dobrygin, V.V.; Dolgoborodov, A.Y. Investigation of Nickel Aluminide Formed Due to Shock Loading of Aluminum-Nickel Mixtures in Flat Recovery Ampoules. *Combust. Explos. Shock Waves* **2018**, *54*(1): 64-71.
[15] Wong, J.; Larson, E.M.; Holt, J.B.; Waide, P.A.; Rupp, B.; Frahm, R. Time-Resolved X-ray Diffraction Study of Solid Combustion Reactions. *Science* **1990**, *249*(4975): 1406-1409.
[16] Song, I.; Thadhani, N.N. Shock-Induced Chemical Reactions and Synthesis of Nickel Aluminides. *Metall. Trans. A* **1992**, *23*(1): 41-48.
[17] Fischer, S.H.; Grubelich, M.C. *Theoretical Energy Release of Thermites, Intermetallics, and Combustible Metals.* Office of Scientific & Technical Information Technical Reports, US, **1999**.
[18] Turrillas, X.; Mas-Guindal, M.J.; Hansen, T.C.; Rodríguez, M.A. The Thermal Explosion Synthesis of AlNi Monitored by Neutron Thermodiffractometry. *Acta Mater.* **2010**, *58*(7): 2769-2777.
[19] Merzhanov, A.G.; Gordopolov, Y.A.; Trofimov, V.S. On the Possibility of Gas Free Detonation in Condensed Systems. *Shock Waves* **1996**, *6*: 157-159.

[20] Gordopolov, Y.A.; Batsanov, S.S.; Trofimov, V.S. Shock-Induced Solid-Solid Reactions and Detonations. In: *Shock Wave Science and Technology Reference Library,* Vol. 4, (Zhang, F., Ed.) Springer-Verlag, Berlin/Heidelberg, **2009**, pp. 287-314; ISBN 978-3-540-88446-0.
[21] Guo, H.; Zheng, Y.; Yu, Q.; Ge, C.; Wang, H. Penetration Behavior of Reactive Liner Shaped Charge Jet Impacting Thick Steel Plates. *Int. J. Impact Eng*. **2019**, *126*: 76-84.
[22] Guo, H.; Xie, J.; Wang, H.; Yu, Q.; Zheng, Y. Penetration Behavior of High-Density Reactive Material Liner Shaped Charge. *Materials* **2019**, *12*(21), paper 3486: 1-14.
[23] Byun, G.; Kim, J.; Lee, C.; Kim, S.J.; Lee, S. Kinetic Spraying Deposition of Reactive-Enhanced Al-Ni Composite for Shaped Charge Liner Applications. *J. Therm. Spray Techn.* **2016**, *25*(3): 483-493.
[24] Lee, S.; Kim, J.; Kim, S.; Lee, S.; Jeong, J.; Lee, C. Performance Comparison of Double-Layer Liner for Shaped Charge Fabricated Using Kinetic Spray. *J. Therm. Spray Techn.* **2019**, *28*(3): 484-494.
[25] Sun, M.; Li, C.; Zhang, X.; Hu, X.; Hu, X.; Liu, Y. Reactivity and Penetration Performance Ni-Al and Cu-Ni-Al Mixtures as Shaped Charge Liner. *Materials* **2018**, *11*(11), paper 2267: 1-11.
[26] Yin, Z.; Ma, C.; Li, S.; Cheng, G. Perforation of an Ultra-High Strength Steel Penetrated by Shaped Charge Jet. *Mater. Sci. Eng. A* **2004**, *379*(1-2): 443-447.
[27] Voitenko, Y.I.; Zakusylo, R.V.; Wojewódka, A.T.; Gontar, P.A.; Gerlich, M.M.; Drachuk, O.G. New Functional Materials in Mechanical Engineering and Geology. *Cent. Eur. J. Energ. Mat*. **2019**, *16*(1): 135-149.
[28] Bai, X.; Liu, J.; Li, S.; Lv, C.; Guo, W.; Wu, T. Effect of Interaction Mechanism between Jet and Target on Penetration Performance of Shaped Charge Liner. *Mater. Sci. Eng. A* **2012**, *553*(15): 142-148.
[29] Bassim, M.; Boakye-Yiadom, S.; Bolduc, M. Microstructural Evolution from Shaped Charge through Steel Plates. *Appl. Mech. Mater.* **2014**, *566*: 344-349.
[30] Lambert, D. Re-Visiting 1-D Hypervelocity Penetration. *Int. J. Impact Eng*. **2008**, *35*(12): 1631-1635.
[31] Bai, Y.; Cheng, C.; Yu, S. On Evolution of Thermo-Plastic Shear Band. *Acta Mech. Sinica-Prc*. **1986**, *2*(1): 1-7.

Received: December 27, 2020
Revised: June 18, 2021
First published online: June 30, 2021